


## PAPER

[View Article Online](#)  
[View Journal](#) | [View Issue](#)Cite this: *Mater. Adv.*, 2022,  
3, 7248Lead-free AgBiI<sub>4</sub> perovskite artificial synapses for  
a tactile sensory neuron system with information  
preprocessing function†Haibo Ye,<sup>a</sup> Zhiyong Liu,<sup>\*a</sup> Hangdi Han,<sup>a</sup> Tielin Shi<sup>a</sup> and Guanglan Liao<sup>ab</sup> 

Organometal halide perovskites (OHPs) exhibit great potential in memristors and artificial synaptic devices. However, the toxicity of lead and instability set barriers for further applications in neuromorphic computing. Herein, we demonstrate an artificial synapse based on inorganic lead-free AgBiI<sub>4</sub> perovskites, which exhibits typical analog resistive switching (RS) characteristics and synaptic behaviors. Several functions of biological synapses are realized including long-term potentiation (LTP), long-term depression (LTD), paired-pulse facilitation (PPF) and spike-timing-dependent plasticity (STDP). Furthermore, by integrating a tactile sensor array with a AgBiI<sub>4</sub> synaptic device, an artificial sensory neuron system is demonstrated. Under pressure stimulations with various intensities, an electrical pre-synaptic signal is transferred to artificial synapses for further information preprocessing, realizing the capability of contrast enhancement and noise reduction. After information preprocessing with an artificial sensory neuron system, the recognition accuracy reaches up to almost 100% with only 500 training epochs by using the MNIST handwritten data set. The presented work provides a new candidate for the next generation of neuromorphic computation based on lead free perovskites.

Received 12th June 2022,  
Accepted 28th July 2022

DOI: 10.1039/d2ma00675h

[rsc.li/materials-advances](https://rsc.li/materials-advances)

## 1. Introduction

With the increasing requirements of fast processing of large amounts of data and information in sensing systems, traditional von Neumann architecture, where the data transfer speed between the central processing unit and the memory is limited, is facing severe constraints such as Moore's law limit, storage walls, and high energy consumption.<sup>1,2</sup> The human brain composed of a high-density synapse network is capable of highly parallel information processing.<sup>3,4</sup> Thus, building a computer architecture similar to the human brain nervous system is considered to be promising for overcoming the limitations of von Neumann computing systems. Neuromorphic computing systems composed of electronic neurons and synapses achieve a high degree of parallelism with the physically united memory and processing units. Among them, the artificial synapse is the fundamental unit in the neuromorphic computing system, which is able to emulate essential synaptic functions in a single electronic device, which

consumes only femtojoule-level amounts of energy.<sup>4–7</sup> In a sensing system, integrating sensors with artificial synapses with short-term plasticity and long-term plasticity instead of conventional complementary metal-oxide semiconductor (CMOS) circuits not only reduces the amount of hardware and power consumption but also achieves first-stage data processing function and boosts the data transfer speed.<sup>8–10</sup> The next-generation synaptic devices are concentrated on metal oxide semiconductors,<sup>11</sup> organic semiconductors,<sup>12</sup> and 2D materials,<sup>13</sup> where tradeoffs are always required between the advantages and associated shortcomings.

In the last few years, organometal halide perovskites (OHPs) have attracted large amounts of attention for their remarkable performance in solar cells, which is attributed to their outstanding material properties (strong optical absorption, tunable band gap, ambipolar charge transport, and long electron-hole diffusion length).<sup>14–24</sup> In 2020, Zeng *et al.* reported a blade-coated perovskite solar cell with a self-assembled monolayer, achieving a power conversion efficiency of 14.13%.<sup>25</sup> In addition to the application in solar cells, OHPs also have great potential in an artificial synaptic device. In 2015, Xu *et al.* reported the first artificial synapse based CH<sub>3</sub>NH<sub>3</sub>PbBr<sub>3</sub> perovskite, emulating important synaptic characteristics in a single electronic device successfully.<sup>4</sup> Since then, a variety of OHP artificial synapses have been reported.<sup>10,26–30</sup> In 2020, Pi *et al.* reported an optically stimulated synaptic device based on the hybrid structure of

<sup>a</sup> State Key Laboratory of Digital Manufacturing Equipment and Technology, Huazhong University of Science and Technology, Wuhan, 430074, China.  
E-mail: zhiyong\_liu@hust.edu.cn

<sup>b</sup> Shenzhen Huazhong University of Science and Technology Research Institute, Shenzhen, 518057, China

† Electronic supplementary information (ESI) available. See DOI: <https://doi.org/10.1039/d2ma00675h>



silicon nanomembranes and perovskites, which has great potential in the field of multi-functional and low energy consumption synaptic devices.<sup>31–33</sup> However, the toxicity of lead and the intrinsic instability caused by the organic group in OHPs limit the further practical and commercial application of OHP-based artificial synapses in neuromorphic computing. Consequently, it is absolutely necessary to further explore the non- or low-toxicity and stable perovskite material to promote the commercial applications of perovskite artificial synapses.<sup>31,34–36</sup> To solve this problem, large amounts of efforts such as  $\text{Sn}^{2+}$ ,  $\text{Ge}^{2+}$ ,  $\text{Bi}^{3+}$  and  $\text{Sb}^{3+}$ <sup>37–40</sup> have been taken. However, the intrinsic instability of Sn or Ge caused by the easy oxidation of  $\text{Sn}^{2+}$  to  $\text{Sn}^{4+}$  or  $\text{Ge}^{2+}$  to  $\text{Ge}^{4+}$  when being exposed to ambient air still has not been solved well.<sup>41,42</sup> Low-toxicity and stable  $\text{Bi}^{3+}$  and  $\text{Sb}^{3+}$  represent another candidate to replace Pb, offering a similar ionic radius and identical electronic structure to  $\text{Pb}^{2+}$ . Recently, a perovskite compound  $\text{A}_3\text{B}_2\text{X}_9$  ( $\text{B} = \text{Bi}, \text{Sb}$ ) is studied for lead-substitution. Hu *et al.* have reported a flexible memristor based on  $\text{Cs}_3\text{Bi}_2\text{I}_9$  perovskites.<sup>43</sup> Paramanik *et al.* studied the resistive switching (RS) and artificial synaptic behaviors in layered  $\text{Cs}_3\text{Sb}_2\text{I}_9$  lead-free perovskites.<sup>44</sup> Nevertheless, the structure of the  $\text{A}_3\text{B}_2\text{X}_9$  perovskite exhibits low-dimensional (0 and 2D) and demonstrates unfavorable optoelectronic properties.<sup>45</sup> The Ag–Bi–I ternary family is another promising candidate for lead-free perovskite materials. Lu *et al.* achieved a power conversion efficiency of 2.1% based on the  $\text{AgBiI}_4$  perovskite.<sup>46</sup> Pecunia *et al.* fabricated the near-infrared (NIR)-blind visible light photodetection based on  $\text{Ag}_2\text{BiI}_5$ .<sup>47</sup> In our previous work, we have reported a lead-free  $\text{AgBiI}_4$  flexible memristor with an ultralow operating voltage of 0.16 V.<sup>48</sup> However, to the best of our knowledge, there is no relevant report on the application of the Ag–Bi–I ternary family in the field of artificial synapses.

In this work, we demonstrate an artificial synapse based on the lead-free inorganic  $\text{AgBiI}_4$  perovskite with a structure of Ag/polymethylmethacrylate (PMMA)/ $\text{AgBiI}_4$ /FTO. The synaptic devices exhibit typical bipolar analog RS characteristics and various functions of biological synapses are realized such as long-term potentiation (LTP), long-term depression (LTD), paired-pulse facilitation (PPF) and spike-timing-dependent plasticity (STDP). After integrating the  $\text{AgBiI}_4$  synaptic device with a tactile sensor, an artificial sensory neuron system is demonstrated which can respond to the pressure stimulations with various intensities and realize the capability of contrast enhancement and noise reduction. For Modified National Institute of Standards and Technology (MNIST) data set image recognition, the simulation results show that the device achieves an accuracy of almost 100% with the artificial sensory neuron system after only 500 training epochs, higher than the accuracy of 98% without information preprocessing.

## 2. Results and discussion

The artificial synaptic devices are fabricated based on the lead-free  $\text{AgBiI}_4$  perovskite with a structure of Ag/PMMA/ $\text{AgBiI}_4$ /FTO (Fig. 1a). The insertion of the PMMA layer is to protect the

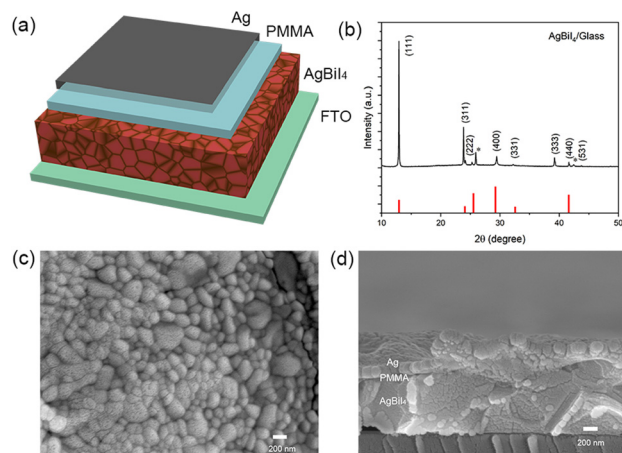


Fig. 1 (a) Schematic illustration of the  $\text{AgBiI}_4$  artificial synapse structure. (b) The experimental and reference (red lines) XRD patterns of the as-prepared  $\text{AgBiI}_4$  perovskite layer. (c) The top-view SEM image of the  $\text{AgBiI}_4$  perovskite layer. (d) The cross-sectional SEM image of the whole device.

$\text{AgBiI}_4$  perovskite film from the diffusion of the metal electrode layer. Besides, the direct contact of Ag and perovskite would result in the formation of a layer of  $\text{AgI}_x$  at the interface, affecting the RS characteristics of the synapse devices.<sup>49</sup> The  $\text{AgBiI}_4$  perovskite film is synthesized by a hot casting method.<sup>50</sup> In brief, the precursor solution is spin-coated on the preheated FTO substrate, followed by the anti-solvent treatment. The temperature of the substrate is a key parameter to obtain high quality and pinhole-free films. The insufficient temperature would result in poor film coverage. Besides, the thickness of the film also highly depends on the preheated temperature. It is reported that substrate preheat treatment will significantly increase the thickness of the  $\text{CsPbIBr}_2$  perovskite.<sup>51</sup> Similarly, a higher preheating temperature will promote the evaporation of the solvent and facilitate the formation of high quality and thick  $\text{AgBiI}_4$  layer. Fig. 1b depicts the X-ray diffraction (XRD) patterns of the  $\text{AgBiI}_4$  film. Strong diffraction peaks at  $12.75^\circ$ ,  $23.94^\circ$ ,  $25.76^\circ$ ,  $29.29^\circ$  and  $41.43^\circ$  can be assigned to the (111), (311), (222), (400) and (440) planes of the  $\text{AgBiI}_4$  cubic-phase structure.<sup>52</sup> Peaks marked as \* imply the existence of  $\text{Ag}_2\text{BiI}_5$ . The top-view scanning electron microscopy (SEM) image of the  $\text{AgBiI}_4$  film is shown in Fig. 1c. The as-prepared film is dense and non-porous with an average grain size of approximately 150 nm. The energy-dispersive X-ray spectra (EDS) in Fig. S1 (ESI†) clearly indicate that the Ag, Bi and I elements are uniformly distributed on the surface of the film. The cross-sectional scanning electron microscope (SEM) image of the whole device depicted in Fig. 1d demonstrates a well-defined layer-by-layer structure with sharp interfaces. The PMMA layer introduced between the perovskite layer and the Ag electrode is too thin to observe. The thickness of the  $\text{AgBiI}_4$  perovskite layer is about 1  $\mu\text{m}$ . The atomic force microscopy (AFM) characterization is further performed to characterize the surface morphology (Fig. S2, ESI†). The root mean square (RMS) roughness is calculated to be 36.2 nm. The X-ray photoelectron spectroscopy (XPS) test is also conducted to study the elemental

compositions in the AgBiI<sub>4</sub> films. The XPS spectrum shows the presence of Ag, Bi, and I (Fig. S3, ESI<sup>†</sup>). As shown in Table S1 (ESI<sup>†</sup>), the atomic percentages of Ag, Bi, and I are 9.18, 9.44, and 42.38%, indicating that the atomic ratio of Ag, Bi, and I on perovskite films is around 1 : 1 : 4.

The RS characteristics are investigated by analyzing the current–voltage (*I*–*V*) curves of the Ag/PMMA/AgBiI<sub>4</sub>/FTO devices. The *I*–*V* curve is carried out in the DC sweeping mode. An external bias sweeping in a routine of 0 → 3.0 → 0 → −3.0 → 0 V is applied to the Ag electrode with the grounded FTO electrode. A current compliance of 0.01 A is set up to prevent the permanent breakdown of the device. As shown in Fig. 2a, the device is set at a high resistance state (HRS) before the voltage sweep. When a positive voltage sweep (0 → 3.0 V → 0 V) is applied on the Ag electrode, the device is switched to the LRS and remains in the LRS during the reverse voltage sweep. The resistance state of the device is reversed from the HRS to the LRS when a negative voltage sweep (0 → −3.0 V → 0 V) is applied. To investigate the role of the PMMA layer in the RS

behavior of synaptic devices, the *I*–*V* characteristic of the PMMA layer with a structure of ITO/PMMA/Ag is performed. The PMMA layer shows no RS behavior under cyclic scanning from 1 V to −1 V and has little effect on the RS behavior of the synaptic devices (Fig. S4a, ESI<sup>†</sup>). The ultrathin PMMA layer acts as a protective layer not only avoiding the reaction of the perovskite film with the top electrode but also protecting the perovskite film from moisture and oxygen under ambient conditions. The device without the PMMA layer exhibits a similar RS behavior and a higher ON/OFF ratio (Fig. S4b, ESI<sup>†</sup>). This can be attributed to the formation of AgI<sub>x</sub> between the Ag electrode and the AgBiI<sub>4</sub> layer. The double logarithmic scale of the *I*–*V* curve in the positive sweep is shown in Fig. S5 (ESI<sup>†</sup>). In the HRS, the slope fitted by the curve is 1.08 and 2.39, displaying an ohmic region and a Child's law region, respectively, where the space charge limited current (SCLC) conduction occurs. In the LRS, a slope of 1.19 corresponds to an ohmic region indicating the formation of conductive filaments in this transition process. A previous study has demonstrated that the



Fig. 2 (a) Typical current–voltage (*I*–*V*) curve of the AgBiI<sub>4</sub> artificial synapse under positive and negative sweeps. (b) *I*–*V* curves under 10 positive and 10 negative voltage sweeps (0 → 1.5 → 0 → −1.0 → 0 V). (c) The EPSC plasticity with positive pulses (1.5 V, 0.1 s). (d) The EPSC plasticity with negative pulses (−1.5 V, 0.1 s).



Ag filaments play a leading role in the RS process of AgBiI<sub>4</sub> memristor.<sup>48</sup> However, the thickness of the AgBiI<sub>4</sub> layer reaches up to almost 1 μm in this study and the RS characteristic is totally different from the previous study. It is worth noting that the thickness of the medium layer also plays a significant role in the mechanism of RS, where two types of conductive filaments can coexist in a single memory cell.<sup>53</sup> Here, we suppose that when the thickness of the medium layer becomes larger, the I vacancy defects (*V<sub>I</sub>*) are responsible for the RS mechanism instead of Ag conductive filaments which usually require a larger electric field.<sup>19</sup> The migration of *V<sub>I</sub>* in the AgBiI<sub>4</sub> film causes the formation/rupture of the conductive filaments and the schematic diagram for the RS mechanism is illustrated in Fig. S6 (ESI†). In the initial state, the *V<sub>I</sub>* is evenly distributed in the perovskite film. During the set process, when a positive bias is applied on the Ag top electrode, the *V<sub>I</sub>* tends to migrate to the ITO electrode. *V<sub>I</sub>* filaments may be formed and become connected from the bottom electrode to the top electrode. During the reset process, the *V<sub>I</sub>* tends to migrate to the Ag electrode, resulting in the fracture of *V<sub>I</sub>* filaments.

During the Set process, the resistance of the device decreases continuously from the HRS to the LRS, which is similar to the transmission characteristics of the biological synapse. To assess the consecutively tunable resistance states accurately, smaller continuous voltage sweeps (0 → 1.5 → 0 → −1.5 → 0 V) are applied on the device to carefully control the change of resistances. As shown in Fig. 2b, when 10 consecutive sweeps of positive voltage are applied to the device, the current increases after each sweep. Subsequently, after applying 10 consecutive sweeps of negative voltage, the current gradually decreased with the increase of voltage sweep number. Different from devices that show sudden conductance variation in memristors with binary states, the conductance of the AgBiI<sub>4</sub> device varies gradually under both positive and negative sweeps, implying that the AgBiI<sub>4</sub> device emulates a successively variable synaptic weight. To further evaluate the modulable synaptic plasticity, 100 repeated positive voltage pulses (1.5 V, 0.1 s) are applied to the device for potentiation, followed by 100 negative voltage pulses for depression. As shown in Fig. 2c and d, the excitatory postsynaptic current (EPSC) increases with the increase of the positive pulses and exhibits the opposite change under negative pulses. The modulable synaptic plasticity behaviors resemble the synaptic LTP and LTD processes of the biological synapse. To investigate the stability of the synaptic devices based on the AgBiI<sub>4</sub> perovskite, the unsealed device is put in an ambient environment for 100 days. Fig. S7 (ESI†) shows the LTP and LTD characteristics of the device before and after storage, which confirms the good stability of our AgBiI<sub>4</sub>-based devices.

The biologic synaptic plasticity is a change in synaptic weight in response to stimuli, which serves as a bridge between two neurons to transmit information and is the basis of learning and memory. In the AgBiI<sub>4</sub> perovskite devices, the Ag electrode and the FTO electrode emulate presynaptic and postsynaptic neurons, respectively, realizing the learning and

memory functions of the human brain including STP and LTP by controlling the input voltage. Fig. 3a depicts the spike-duration-dependent plasticity (SDDP) of the AgBiI<sub>4</sub> perovskite synaptic devices. Electrical stimuli with different pulse widths ranging from 0.1 to 1.1 s are applied to the synaptic device. The EPSC peaks increase gradually with the increase of pulse width, implying that a larger synaptic weight will be achieved under a longer-duration pulse. The effect of the voltage amplitude on the synaptic plasticity is also studied (Fig. 3b). With a fixed pulse width, the EPSC increases with the increase of pulse amplitude, indicating that the AgBiI<sub>4</sub> perovskite synaptic device has the function of spike-voltage dependent plasticity (SVDP). Besides, the spike-number dependent plasticity (SNDP) can also be mimicked with different numbers of voltage pulses. As shown in Fig. 3c, the increase in the pulse numbers results in a larger EPSC response.

The spike-frequency dependent plasticity (SFDP) is an important characteristic of synaptic devices, which is related to learning, associative memory, and forgetting. This phenomenon in biological synapses is that the response to the stimuli which comes after the first stimuli will be enhanced within a short interval. Similarly, the change of the synaptic weight in the perovskite synapse also depends on the paired-pulse interval. To evaluate the PPF for STP of the synaptic devices, ten synaptic spikes with various frequencies (1.7, 2.5, 10, 12.5, 16.7, 25, 50 and 100 Hz) are applied to the devices. As shown in Fig. 3d, with the decrease of the spike frequency, the EPSC exhibits a downward trend, indicating that smaller paired-pulse intervals lead to much higher EPSC excited by the second pulse. The PPF index is calculated from the following equation:

$$\text{PPF index} = (A_2 - A_1)/A_1$$

where *A*<sub>1</sub> and *A*<sub>2</sub> are the peak value of the first and second pulse responses, respectively. As shown in Fig. 3e, the PPF index decreases from 30% to 1% as the paired-pulse interval increases from 10 to 600 ms. Furthermore, the data are fitted well with a double-exponential function:<sup>54</sup>

$$y = y_0 + C_1 \exp\left(-\frac{\Delta t}{\tau_1}\right) + C_2 \exp\left(-\frac{\Delta t}{\tau_2}\right)$$

where  $\Delta t$  is the paired-pulse interval, *y*<sub>0</sub> is the resting facilitation magnitude, *C*<sub>1</sub> and *C*<sub>2</sub> are facilitation constants, and  $\tau_1 = 22$  ms and  $\tau_2 = 52$  ms are the characteristic relaxation time.

Another essential function of the synapse is STDP, also known as the Hebbian learning rule, which can evaluate temporal correlations between the pre-synaptic and post-synaptic spikes. Four forms of STDP behaviors have been discovered in the biological synapse, which have different functions regarding information processing and storage. Here the asymmetric Hebbian learning rule is realized, where a post-synaptic spike arriving after the pre-synaptic spike ( $\Delta t > 0$ ,  $\Delta t = t_{\text{post}} - t_{\text{pre}}$ ) will lead to LTP of the synapse and the post-synaptic spike arriving before the pre-synaptic spike ( $\Delta t < 0$ ) leads to LTD. The change of weight ( $\Delta W$ ) in asymmetric







**Fig. 3** (a) The EPSC with the pulse duration from 0.1 to 1.1 s (1.0 V). (b) The EPSC with the pulse voltage amplitude from 0.1 to 1.7 V (0.1 s). (c) SNDP ratio versus pulse number stimulated by different numbers of voltage pulses. (d) The EPSC with a pulse frequency from 1.7 to 100 Hz. (e) PPF index versus time interval between two successive pulses (1.5 V, 0.05 s). Inset: PPF index versus time interval between the 1st and the 10th pulse (1.5 V, 0.05 s). (f) STDP-like behaviors in the AgBiI<sub>4</sub> based artificial synapses. The reading voltage applied above is 0.1 V.

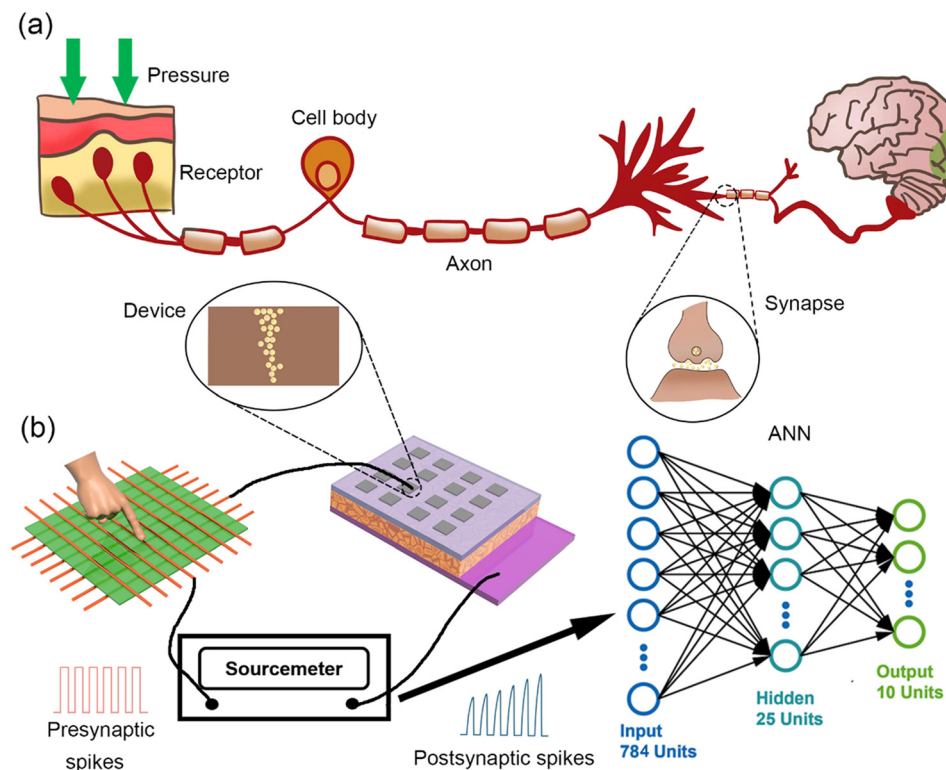


**Fig. 4** (a) Schematic illustration of the biological tactile sensing system. (b) The artificial sensory neuron system consisting of tactile sensors, perovskite artificial synapses and ANNs.



Hebbian can be fitted by the following equation:<sup>55</sup>

$$\Delta W = A \exp\left(-\frac{\Delta t}{\tau}\right) + \Delta W_0$$

where  $A$  and  $\tau$  are the scaling factor and time constant, respectively. As shown in Fig. 3f, the relationship of  $\Delta W$  and  $\Delta t$  are well fitted with the exponential function, indicating that the anti-Hebbian STDP learning rule is successfully simulated in the AgBiI<sub>4</sub> perovskite synaptic devices.

In the human tactile sensing system, the action spikes generated by the mechanoreceptors under tactile input transmit along the afferent axons to synapses. Then, the synapses preprocess the information and relay it to neurons for further processing, as depicted in Fig. 4a. The mechanoreceptors in the skin are able to encode the tactile stimuli as an action potential and the synapse is a connecting bridge between pre- and post-neurons for brain functions such as learning, forgetting, and memory. To emulate the human tactile sensing system, an artificial sensory neuron system is demonstrated by integrating a tactile sensor array with the AgBiI<sub>4</sub> synaptic device. The photographs of the AgBiI<sub>4</sub> artificial synaptic device and the tactile sensor are depicted in Fig. S8 (ESI<sup>†</sup>). The sensor arrays consist of a pressure-sensitive film addressed by a network of orthogonal conductive threads on each side. Each point of overlap between the orthogonal electrodes is sensitive to normal pressure, modulating the resistance through the pressure-sensitive film. The pressure response of a single sensing element is shown in Fig. S9 (ESI<sup>†</sup>), changing from about

750  $\Omega$  (1 N) to 250  $\Omega$  (5 N). In the AgBiI<sub>4</sub> synaptic devices, the TE and BE serve as the pre-synaptic input and the post-synaptic output respectively, while the change of resistance is regarded as the potentiation or depression of the synaptic weight. Therefore, after the pressure signals being transformed in to the pre-synaptic by the sensor array, the changes in synapse resistance can be obtained by the post-synaptic current. Next, the post-synaptic current can be subsequently input into the artificial neural networks (ANNs) which work as the brain for further recognition. Fig. 4b displays the schematic illustration of the artificial sensory neuron system, the tactile sensor is connected with the synaptic device in series. A source-meter is utilized to applied voltage spikes to the tactile sensor and the synaptic device. Finally, the post-synaptic output currents are relayed to the artificial neural network for further processing.

Unlike conventional sensory systems based on the CMOS technology, the synapses in the artificial sensory neural system can directly preprocess the information transmitted from the tactile sensor with reductions in the amount of hardware and power consumption. The information preprocessing of the artificial sensory neuron system is carried out based on pressure-dependent plasticity. Fig. 5a depicts the output current as the function of pressure applied to the mechanoreceptors, where the input pressure intensity is set to be 1.0 N, 1.6 N, 2.6 N and 5.5 N, and the corresponding voltage on the synaptic device is measured to be 0.7 V, 0.9 V, 1.1 V and 1.4 V. The EPSC increases as the pressure increases from 1.0 N to 5.5 N. Then,



**Fig. 5** (a) The EPSC with different pressure. (b) The training process carried out with repeated pressure pulses (repeated 20 times) for the artificial sensory neuron system. (c) The normalization of the current–pressure curve based on the output current of the artificial sensory neuron system. (d) The images of figure 1–9 in the MNIST database. (e) The images of figure 1–9 in the MNIST database after being preprocessed by the artificial sensory neuron system (f) Comparisons of the image recognition accuracy for the MNIST patterns with and without the image preprocessing.



20 repeated voltage spikes are applied to the system to carry out a training process. As shown in Fig. 5b, after repeated training, the difference between the output currents is enlarged according to the different pressures. The increase in the rate of the output current with a higher pressure is higher than that with a lower pressure intensity. The currents with a lower intensity decay faster, whereas the currents with a higher intensity decay slower. In this way, the main feature in one image is highlighted, and the image contrast is enhanced. The relationship between the output current and input pressure is established for the artificial sensory neuron system by fitting the experimental results, where the current and the pressure are normalized from 0 to 1. The data is fitted well with a power function (Fig. 5c):

$$y = ax^b$$

where  $a$  and  $b$  are calculated to be 1 and 2.26, respectively. To further demonstrate the function of information preprocessing, a  $784 \times 25 \times 10$  three-layered fully connected neural network is designed for image recognition with and without the artificial sensory neuron system. The images of figure 1–9 in the MNIST database are used for recognition (Fig. 5d). After preprocessing the data by the artificial sensory neuron system, the results present high-quality background noise reduction for the output image (Fig. 5e). Furthermore, the preprocessed information is transmitted to the neural network for recognition. As shown in Fig. 5f, the recognition accuracy reaches up to almost 100% with 500 training epochs after being preprocessed *via* the artificial sensory neuron system. By contrast, directly recognizing in the neural network results in a recognition accuracy of 99% when training epochs run up to 2000. The above results demonstrate that the artificial sensory neuron system is able to realize the image preprocessing on the hardware level and improve both recognition speed and recognition accuracy for artificial neural networks.

### 3. Conclusion

In summary, an artificial synapse based nontoxic  $\text{AgBiI}_4$  perovskite is successfully fabricated, which exhibits typical bipolar analog RS characteristics. The basic biological synaptic functions such as LTP, LTD, PPF and STDP are successfully mimicked. Furthermore, an artificial sensory neuron system is demonstrated by integrating the synaptic device with tactile sensors, which are capable of information preprocessing and further realizing the functions of contrast enhancement and noise reduction. The pattern recognition accuracy reaches up to almost 100%, higher than the accuracy of 98% without information preprocessing. Our work opens up new avenues for the realization of neuromorphic computation based on lead-free perovskites.

### 4. Experimental section

#### 4.1 Materials

The FTO substrates with a  $14 \Omega \square^{-1}$  resistance (NSG-14) were purchased from Nippon Sheet Glass Co. Ltd., Japan. Anhydrous

ethanol, acetone, and dimethyl sulfoxide (DMSO) were purchased from Sinopharm Chemical Reagent Co., Ltd. The anhydrous chlorobenzene, AgI and  $\text{BiI}_3$  were purchased from Alfa Aesar. The  $N,N$ -dimethylformamide ( $\geq 99.9\%$ ) was purchased from Shanghai Aladdin Biochemical Technology Co. LTD. The polymethylmethacrylate (PMMA) was purchased from Sigma-Aldrich. All materials were used without further purification.

#### 4.2 Device fabrication

The FTO substrates were cleaned in de-ionized (DI) water, acetone and ethanol sequentially and then treated with UV-ozone for 15 min before use. To prepare the perovskite precursor solution, 353.8 mg of  $\text{BiI}_3$  and 140.8 mg of AgI were mixed in the DMF and DMSO mixture (1 : 1). Before depositing the perovskite film, the substrates and the precursor solution were preheated at  $120^\circ\text{C}$ . The precursor solution was spread onto the substrate, followed by spin-coating at 5000 rpm for 30 s. Before the end of the spin-coating process, chlorobenzene (125  $\mu\text{L}$ ) was splashed over the rotating substrate to perform an anti-solvent treatment. Finally, the substrates were annealed at  $150^\circ\text{C}$  for 30 min on a hotplate. After the deposition of the perovskite layer, a solution of PMMA in chlorobenzene (1  $\text{mg mL}^{-1}$ ) was deposited by spin-coating at 4000 rpm for 20 s. The device was then annealed for 5 min. To complete the device,  $0.5 \text{ mm} \times 0.5 \text{ mm}$  top electrodes were deposited on the PMMA by thermal evaporation ( $< 1 \times 10^{-3} \text{ Pa}$ ) using the quartz crystal motion rate.

#### 4.3 Measurement and characterization

X-Ray diffraction (XRD) diagrams were carried out using XRD analysis (PANalytical PW3040/60) with Cu  $K\alpha$  radiation ( $\lambda = 1.5406 \text{ \AA}$ ) from  $10^\circ$  to  $50^\circ$ . The surface morphology of the devices was examined by scanning electron microscopy (SEM, Helios NanoLab G3). The EDS elemental mapping and cross-sectional images of the devices were also examined by scanning electron microscopy. The X-ray photoelectron spectroscopy (XPS) measurement was performed using a photoelectron spectrometer (VG Multilab 2000 X, Thermo Electron Corp., Waltham, MA, USA). The electrical characteristics were measured using an electrochemical station (Autolab PGSTAT302N, Metrohm Autolab, Utrecht, The Netherlands).

### Conflicts of interest

The authors declare no competing financial interest.

### Acknowledgements

The authors acknowledge the financial support from the National Key R&D Program of China (Grant No. 2019YFB1503200), the National Natural Science Foundation of China (Grant no. 51905202 and 51905203), and the fund from the Science, Technology and Innovation Commission of Shenzhen Municipality (Grant No. JCYJ20190809100209531). We appreciate the Analytical and Testing Center and Flexible Electronics Research Center of



Huazhong University of Science and Technology for the XRD and XPS measurements. We also acknowledge the Measurement Laboratory of Collaborative Innovation Center for Digital Intelligent Manufacturing Technology and Application for support in SEM testing.

## References

- 1 P. A. Merolla, J. V. Arthur, R. Alvarez-Icaza, A. S. Cassidy, J. Sawada, F. Akopyan, B. L. Jackson, N. Imam, C. Guo, Y. Nakamura, B. Brezzo, I. Vo, S. K. Esser, R. Appuswamy, B. Taba, A. Amir, M. D. Flickner, W. P. Risk, R. Manohar and D. S. Modha, *Science*, 2014, **345**, 668–673.
- 2 P. M. Sheridan, F. Cai, C. Du, W. Ma, Z. Zhang and W. D. Lu, *Nat. Nanotechnol.*, 2017, **12**, 784–789.
- 3 Y. Van De Burgt, E. Lubberman, E. J. Fuller, S. T. Keene, G. C. Faria, S. Agarwal, M. J. Marinella, A. Alec Talin and A. Salleo, *Nat. Mater.*, 2017, **16**, 414–418.
- 4 W. Xu, H. Cho, Y. H. Kim, Y. T. Kim, C. Wolf, C. G. Park and T. W. Lee, *Adv. Mater.*, 2016, **28**, 5916–5922.
- 5 L. F. Abbott and S. B. Nelson, *Nat. Neurosci.*, 2000, **3**, 1178–1183.
- 6 K. Kim, C. L. Chen, Q. Truong, A. M. Shen and Y. Chen, *Adv. Mater.*, 2013, **25**, 1693–1698.
- 7 B. Tian, L. Liu, M. Yan, J. Wang, Q. Zhao, N. Zhong, P. Xiang, L. Sun, H. Peng, H. Shen, T. Lin, B. Dkhil, X. Meng, J. Chu, X. Tang and C. Duan, *Adv. Electron. Mater.*, 2019, **5**, 1800600.
- 8 F. Zhou, Z. Zhou, J. Chen, T. H. Choy, J. Wang, N. Zhang, Z. Lin, S. Yu, J. Kang, H. S. P. Wong and Y. Chai, *Nat. Nanotechnol.*, 2019, **14**, 776–782.
- 9 C. Zhang, W. Bin Ye, K. Zhou, H. Y. Chen, J. Q. Yang, G. Ding, X. Chen, Y. Zhou, L. Zhou, F. Li and S. T. Han, *Adv. Funct. Mater.*, 2019, **29**, 1–10.
- 10 X. Yang, Z. Xiong, Y. Chen, Y. Ren, L. Zhou, H. Li, Y. Zhou, F. Pan and S. T. Han, *Nano Energy*, 2020, **78**, 105246.
- 11 B. H. P. Wong, F. Ieee, H. Lee, S. Yu, S. M. Ieee, Y. Chen, Y. Wu, P. Chen, B. Lee, F. T. Chen and M. Tsai, *Proc. IEEE*, 2012, **100**, 1951–1970.
- 12 T. Sekitani, T. Yokota, U. Zschieschang, H. Klauk, S. Bauer, K. Takeuchi, M. Takamiya, T. Sakurai and T. Someya, *Science*, 2009, **326**, 1516–1520.
- 13 T. Roy, M. Tosun, J. S. Kang, A. B. Sachid, S. B. Desai, M. Hettick, C. C. Hu and A. Javey, *ACS Nano*, 2014, **8**, 6259–6264.
- 14 W. Nie, H. Tsai, R. Asadpour, J.-C. Blancon, A. J. Neukirch, G. Gupta, J. J. Crochet, M. Chhowalla, S. Tretiak, M. A. Alam, H.-L. Wang and A. D. Mohite, *Science*, 2015, **347**, 522–525.
- 15 W. S. Yang, J. H. Noh, N. J. Jeon, Y. C. Kim, S. Ryu, J. Seo and S. Il Seok, *Science*, 2015, **348**, 1234–1237.
- 16 Z.-K. Tan, R. S. Moghaddam, M. L. Lai, P. Docampo, R. Higler, F. Deschler, M. Price, A. Sadhanala, L. M. Pazos, D. Credgington, F. Hanusch, T. Bein, H. J. Snaith and R. H. Friend, *Nat. Nanotechnol.*, 2014, **9**, 687–692.
- 17 D. B. Mitzi, C. D. Dimitrakopoulos and L. L. Kosbar, *Chem. Mater.*, 2001, **13**, 3728–3740.
- 18 M. Anaya, W. Zhang, B. C. Hames, Y. Li, F. Fabregat-Santiago, M. E. Calvo, H. J. Snaith, H. Míguez and I. Mora-Seró, *J. Mater. Chem. C*, 2017, **5**, 634–644.
- 19 J. Choi, S. Park, J. Lee, K. Hong, D. H. Kim, C. W. Moon, G. Do Park, J. Suh, J. Hwang, S. Y. Kim, H. S. Jung, N. G. Park, S. Han, K. T. Nam and H. W. Jang, *Adv. Mater.*, 2016, 6562–6567.
- 20 G. Xing, N. Mathews, S. Sun, S. S. Lim, Y. M. Lam, M. Gratzel, S. Mhaisalkar and T. C. Sum, *Science*, 2013, **342**, 344–347.
- 21 M. M. Lee, J. Teuscher, T. Miyasaka, T. N. Murakami and H. J. Snaith, *Science*, 2012, **338**, 643–647.
- 22 H. Ye, Z. Liu, X. Liu, B. Sun, X. Tan, Y. Tu, T. Shi, Z. Tang and G. Liao, *Appl. Surf. Sci.*, 2019, **478**, 417–425.
- 23 B. Li, Z. Li, X. Wu and Z. Zhu, *Nano Res. Energy*, 2022, DOI: [10.26599/NRE.2022.9120011](https://doi.org/10.26599/NRE.2022.9120011).
- 24 B. Wang, J. Ma, Z. Li, G. Chen, Q. Gu, S. Chen, Y. Zhang, Y. Song, J. Chen, X. Pi, X. Yu and D. Yang, *Nano Res.*, 2022, **15**, 1069–1078.
- 25 J. Zeng, L. Bi, Y. Cheng, B. Xu and A. K.-Y. Jen, *Nano Res. Energy*, 2022, **1**, DOI: [10.26599/NRE.2022.9120004](https://doi.org/10.26599/NRE.2022.9120004).
- 26 S. G. Kim, Q. Van Le, J. S. Han, H. Kim, M. J. Choi, S. A. Lee, T. L. Kim, S. B. Kim, S. Y. Kim and H. W. Jang, *Adv. Funct. Mater.*, 2019, **29**, 1–11.
- 27 J. Lao, W. Xu, C. Jiang, N. Zhong, B. Tian, H. Lin, C. Luo, J. Travas-Sejdic, H. Peng and C. G. Duan, *J. Mater. Chem. C*, 2021, **9**, 5706–5712.
- 28 R. A. John, N. Yantara, Y. F. Ng, G. Narasimman, E. Mosconi, D. Meggiolaro, M. R. Kulkarni, P. K. Gopalakrishnan, C. A. Nguyen, F. De Angelis, S. G. Mhaisalkar, A. Basu and N. Mathews, *Adv. Mater.*, 2018, **30**, 1–8.
- 29 J. Lao, W. Xu, C. Jiang, N. Zhong, B. Tian, H. Lin, C. Luo, J. Travas-Sejdic, H. Peng and C. G. Duan, *Adv. Electron. Mater.*, 2021, **7**, 2100291.
- 30 Z. Xiao and J. Huang, *Adv. Electron. Mater.*, 2016, **2**, 1–8.
- 31 H. Luo, P. Li, J. Ma, L. Han, Y. Zhang and Y. Song, *Adv. Energy Mater.*, 2022, 2201242.
- 32 Y. Zhu, W. Huang, Y. He, L. Yin, Y. Zhang, D. Yang and X. Pi, *Research*, 2020, **2020**, 1–9.
- 33 W. Huang, P. Hang, Y. Wang, K. Wang, S. Han, Z. Chen, W. Peng, Y. Zhu, M. Xu, Y. Zhang, Y. Fang, X. Yu, D. Yang and X. Pi, *Nano Energy*, 2020, **73**, 104790.
- 34 N.-G. Park, M. Grätzel, T. Miyasaka, K. Zhu and K. Emery, *Nat. Energy*, 2016, **1**, 16152.
- 35 G. Chen, P. Li, T. Xue, M. Su, J. Ma, Y. Zhang, T. Wu, L. Han, M. Aldamasy, M. Li, Z. Li, J. Ma, S. Chen, Y. Zhao, F. Wang and Y. Song, *Small*, 2021, **17**, 1–11.
- 36 J. Ma, M. Qin, P. Li, L. Han, Y. Zhang and Y. Song, *Energy Environ. Sci.*, 2022, **15**, 413–438.
- 37 F. Hao, C. C. Stoumpos, D. H. Cao, R. P. H. Chang and M. G. Kanatzidis, *Nat. Photonics*, 2014, **8**, 489–494.
- 38 G. M. Kim, A. Ishii, S. Öz and T. Miyasaka, *Adv. Energy Mater.*, 2020, **10**, 1–8.
- 39 Z. Tan, J. Li, C. Zhang, Z. Li, Q. Hu, Z. Xiao, T. Kamiya, H. Hosono, G. Niu, E. Lifshitz, Y. Cheng and J. Tang, *Adv. Funct. Mater.*, 2018, **28**, 1–10.





- 40 J. M. Yang, E. S. Choi, S. Y. Kim, J. H. Kim, J. H. Park and N. G. Park, *Nanoscale*, 2019, **11**, 6453–6461.
- 41 F. Wang, J. Ma, F. Xie, L. Li, J. Chen, J. Fan and N. Zhao, *Adv. Funct. Mater.*, 2016, **26**, 3417–3423.
- 42 X. Wang, T. Zhang, Y. Lou and Y. Zhao, *Mater. Chem. Front.*, 2019, **3**, 365–375.
- 43 Y. Hu, S. Zhang, X. Miao, L. Su, F. Bai, T. Qiu, J. Liu and G. Yuan, *Adv. Mater. Interfaces*, 2017, **4**, 1–8.
- 44 S. Paramanik, A. Maiti, S. Chatterjee and A. J. Pal, *Adv. Electron. Mater.*, 2022, **8**, 2100237.
- 45 M. Xia, J. H. Yuan, G. Niu, X. Du, L. Yin, W. Pan, J. Luo, Z. Li, H. Zhao, K. H. Xue, X. Miao and J. Tang, *Adv. Funct. Mater.*, 2020, **30**, 2–9.
- 46 M. Shang, C. Lu, L. Han, Y. Zhu, X. Gan, J. Zhang, D. Hou, H. Sun, Y. Li and Z. Hu, *ACS Appl. Energy Mater.*, 2018, **1**, 4485–4492.
- 47 V. Pecunia, Y. Yuan, J. Zhao, K. Xia, Y. Wang, S. Duhm, L. Portilla and F. Li, *Nano-Micro Lett.*, 2020, **12**, 1–12.
- 48 H. Ye, B. Sun, Z. Wang, Z. Liu, X. Zhang, X. Tan, T. Shi, Z. Tang and G. Liao, *J. Mater. Chem. C*, 2020, **8**, 14155–14163.
- 49 X. Zhu, J. Lee and W. D. Lu, *Adv. Mater.*, 2017, **29**, 1–8.
- 50 T. Baikie, S. Mhaisalkar, B. Ghosh, X. Guo, R. A. John, T. C. Sum, P. C. Harikesh, B. Wu, Arramel, C. Guet, N. Mathews and A. T. S. Wee, *Adv. Energy Mater.*, 2018, **8**, 1802051.
- 51 J. Pan, X. Zhang, Y. Zheng and W. Xiang, *Sol. Energy Mater. Sol. Cells*, 2021, **221**, 110878.
- 52 C. Lu, J. Zhang, H. Sun, D. Hou, X. Gan, M. H. Shang, Y. Li, Z. Hu, Y. Zhu and L. Han, *ACS Appl. Energy Mater.*, 2018, **1**, 4485–4492.
- 53 Y. Sun, M. Tai, C. Song, Z. Wang, J. Yin, F. Li, H. Wu, F. Zeng, H. Lin and F. Pan, *J. Phys. Chem. C*, 2018, **122**, 6431–6436.
- 54 J. Gong, H. Yu, X. Zhou, H. Wei, M. Ma, H. Han, S. Zhang, Y. Ni, Y. Li and W. Xu, *Adv. Funct. Mater.*, 2020, **30**, 1–10.
- 55 N. Caporale and Y. Dan, *Annu. Rev. Neurosci.*, 2008, **31**, 25–46.

